Autonomous methane seep site monitoring offshore Western Svalbard: Hourly to seasonal variability and associated oceanographic parameters

Knut Ola Dølven[1], Bénédicte Ferré[1], Anna Silyakova[1], Pär Jansson[2,*], Peter Linke[3,*], and Manuel Moser[1,*]

[1]Centre for Arctic Gas Hydrate, Environment, and Climate,UiT The Arctic University of Norway, 9019 Tromsø, Norway
[2]Multiconsult Kyst og Marin, 9013 Tromsø, Norway
[3]GEOMAR Helmholtz Centre for Ocean Research Kiel, 24148 Kiel, Germany
[*]These authors contributed equally to this work

Correspondence: Knut Ola Dølven (knut.o.dolven@uit.no)

Abstract. Improved quantification techniques of natural sources is needed to explain variations in atmospheric methane. In polar regions, high uncertainties in current estimates of methane release from the seabed remain. We present two unique 10 and 3 months long time-series of bottom water measurements of physical and chemical parameters from two autonomous ocean observatories deployed at separate intense seabed methane seep sites (91 and 246m depth), offshore Western Svalbard from 2015 to 2016. Results show high short term (100-1000 nmol L^{-1} within hours) and seasonal variation, as well as higher (2-7 times) methane concentrations compared to previous measurements. Rapid variability is explained by uneven distribution of seepage and changing ocean current directions. No overt influence of tidal hydrostatic pressure or water temperature variations on methane concentration was observed, but an observed negative correlation with temperature at the 246 site fits with hypothesized seasonal blocking of lateral methane pathways in the sediments. Negative correlation between bottom water methane concentration/variability and wind forcing, concomitant with signs of weaker water column stratification indicates increased potential for methane release to the atmosphere in fall/winter. We highlight uncertainties in methane inventory estimates based on discrete water sampling and present new information about short- and long-term methane variability which can help constrain future estimates of seabed methane seepage.

1 Introduction

Unexplained changes in atmospheric methane (CH_4) mole fraction motivates research in understanding and quantifying non-anthropogenic sources (Saunois et al., 2020). The atmospheric forcing of CH_4 is particularly sensitive to changes in emission rates due to a high warming potential and short lifetime. Improved knowledge about atmospheric CH_4 fluxes is therefore crucial to constrain future climate projections (Pachauri and Meyer, 2014; Myhre et al., 2016b). These properties of atmospheric CH_4 also makes reduced anthropogenic CH_4 emissions a potential solution for rapid climate change mitigation (Saunois et al., 2016). A global global effort to cut greenhouse gas emissions through international agreements is, however, dependant on precise estimates of sources and sinks to verify contributions from different nations.

Seabed seepages is considered a minor source of atmospheric CH_4, but with high uncertainty in current and predicted emission estimates (Saunois et al., 2016). Current estimates suggest a total contribution of 7 (5-10) Tg y^{-1} (Etiope et al., 2019; Saunois et al., 2020), which is ~1% of the total CH_4 emissions to the atmosphere. Methane is released from the seabed as

25   free gas (bubbles) and dissolved gas in sediment pore water. Bubbles rise quickly towards the sea surface, but most CH_4 dissolves near the seafloor because of gas exchange across the bubble rims and bubble dissolution (McGinnis et al., 2006; Jansson et al., 2019a). Dissolved CH_4 is dispersed and advected by ocean currents (Silyakova et al., 2020) and is continuously transformed to carbon dioxide (CO_2) by bacterial aerobic oxidation (Hanson and Hanson, 1996; Reeburgh, 2007). These processes significantly limit the lifetime of CH_4 in the water column and the amount of CH_4 that can reach the atmosphere

30   is highly dependent on the depth where the seepage occurs (McGinnis et al., 2006; Graves et al., 2015). Intense CH_4 seepage at shallow depths in coastal areas and on continental shelves is therefore the main potential source of seabed CH_4 to the atmosphere.

The shallow continental margins of the Arctic Ocean store large amounts of CH_4 as free gas, gas dissolved in pore water fluid, and gas hydrates (Ruppel and Kessler, 2017), i.e. clathrate structures composed of water trapped by hydrocarbon

35   molecules formed and kept stable at low temperature and high pressure (Sloan, 1998). Methane trapped in hydrates or in subsea permafrost, as well as hydrate sealed free gas reservoirs can be destabilized by increasing bottom water temperature, resulting in a potential positive climate feedback loop (Westbrook et al., 2009; Shakhova et al., 2010; Ruppel and Kessler, 2017).

Studies on CH_4 inventory, distribution and release in the Arctic Ocean are mainly based on research cruise data from late

40   spring to early fall, when ice and weather conditions allow field work in the region (Gentz et al., 2014; Sahling et al., 2014; Mau et al., 2017), whereas winter data is sparse. Bottom water temperature (Westbrook et al., 2009; Reagan et al., 2011; Ferré et al., 2012; Braga et al., 2020), water mass origins (Steinle et al., 2015), micro-seismicity (Franek et al., 2017), and hydrostatic pressure (Linke et al., 2009; Römer et al., 2016) have all been proposed to be linked with sources and sinks of CH_4 in the water column. These processes act on a wide range of time-scales, from hours (e.g. hydrostatic pressure) to decades (bottom

45   water temperature). Without a better understanding of the spatial and temporal variability of CH_4 in Arctic Seep sites, it is challenging to untangle these processes. Unconstrained local variability in CH_4 seepage and concentration also imposes a high degree of uncertainty on CH_4 inventory estimates (Saunois et al., 2020). The combination of climate sensitive CH_4 storages, vast shallow ocean regions and limited data availability highlight the need for more understanding of seabed CH_4 seepage on Arctic shelves.

50   To assess the aforementioned challenges, we have obtained, analyzed and compared unique year-round underwater multi-parameter time series from two seafloor observatories deployed at two intense CH_4 seep sites on the western Svalbard continental shelf (Figure 1) where no CH_4 measurements have previously been done in winter season. We combine high frequency physical (ocean currents, temperature, salinity, pressure) and chemical (O_2, CO_2, CH_4) data to perform hypothesis testing and provide new insights on CH_4 distribution, content, as well as variability on short (minutes) and long (seasonal) timescales.

1.1 Regional Settings

Two observatories (O_{91} and O_{246}) were deployed from June 2015 (CAGE 15-3 cruise) to May 2016 (CAGE 16-4 cruise) from R/V *Helmer Hanssen* at the inter-trough shelf region between Isfjorden and Kongsfjorden, west of Prins Karls Forland (PKF). The O_{91} observatory was deployed at 91 m water depth on the continental shelf (78.561^{o}N, 10.142^{o}E) and the O_{246} observatory was deployed at 246 m water depth further offshore close to the shelf break (78.655^{o}N, 9.433^{o}E, Figure 1).

Both sites were located in areas with thousands of previously mapped CH_4 gas seeps (e.g. (Sahling et al., 2014; Veloso-Alarcón et al., 2019; Silyakova et al., 2020), this work, see Figure 1), often referred as "flares" due to the appearance of bubble streams in echo-sounder data. Nonetheless, atmospheric sampling in this region suggests that any emissions to the atmosphere are small (Platt et al., 2018). Gas accumulation at the O_{246} seep site has been suggested to be a result of gas migration in permeable layers within the seabed from deeper free gas or hydrate reservoirs (Rajan et al., 2012; Sarkar et al., 2012; Veloso-Alarcón et al., 2019), while seepage at site O_{91} has been attributed to thawing sub-sea permafrost due to ice sheet retreat at the end of the last glaciation (Sahling et al., 2014; Portnov et al., 2016). Water sampling have indicated high temporal variability with bottom water concentrations (average) changing from 200 nmol L^{-1} within 1 week in July 2014 at O_{91} (Myhre et al., 2016a) and $\sim$ 80 nmol L^{-1} within 20 hours (two single point measurements) at O_{246} in August 2010 (Gentz et al., 2014). A consistent pattern of decreasing concentrations from the sea floor to the sea surface at both sites (400 to <8 nmol L^{-1} at O_{91} (Myhre et al., 2016a)) and from to >500 to <20 nmol L^{-1} at O_{246} (Gentz et al., 2014)) has also been observed. Further offshore, continuous measurements from a towed fast response underwater laser spectrometer also revealed very high spatial CH_4 variability (Jansson et al., 2019b).

The local water masses are characterized by exchange and convergence of the warm, saline Atlantic Water (AW, Temperature T>3°C and absolute salinity S_A >34.65) in the West Spitsbergen Current (WSC) (Beszczynska-Möller et al., 2012) and the colder, fresher Arctic Water (ArW, -1.5<T<1°C, 34.3<S_A <34.8) in the Coastal Current (CC) (Hopkins, 1991) combined with seasonal cooling, ice formation, and freshwater input from land (Nilsen et al., 2016) (Figure 1). Local mixing rates can be strongly affected by synoptic scale weather systems, causing upwelling and disruption of the front between the two ocean currents (Saloranta and Svendsen, 2001; Cottier et al., 2007). Freshwater input in summer stratifies the water column, while cooling, storm activity and sea ice formation can facilitate vertical mixing in winter (Saloranta and Svendsen, 2001; Nilsen et al., 2016).

2 Methods

The "K-Lander" ocean observatories were designed to monitor CH_4 release and associated physical and chemical parameters in challenging environments (see Appendix A). A launcher equipped with camera and telemetry allowed for safe deployment at a site selected by visual control. Observatory O_{91} recorded data from 2 July 2015 to 6 May 2016, while O_{246} recorded data from 1 July until 3 October 2015, when data recording ceased due to an electrical malfunction.

Both observatories were equipped with an Acoustic Doppler Current Profiler (ADCP), a CTD with oxygen optode, and Contros HydroC CO_2 and CH_4 sensors (see Figure A1 and Table B1). We calculated correlation coefficient (R) matrices to
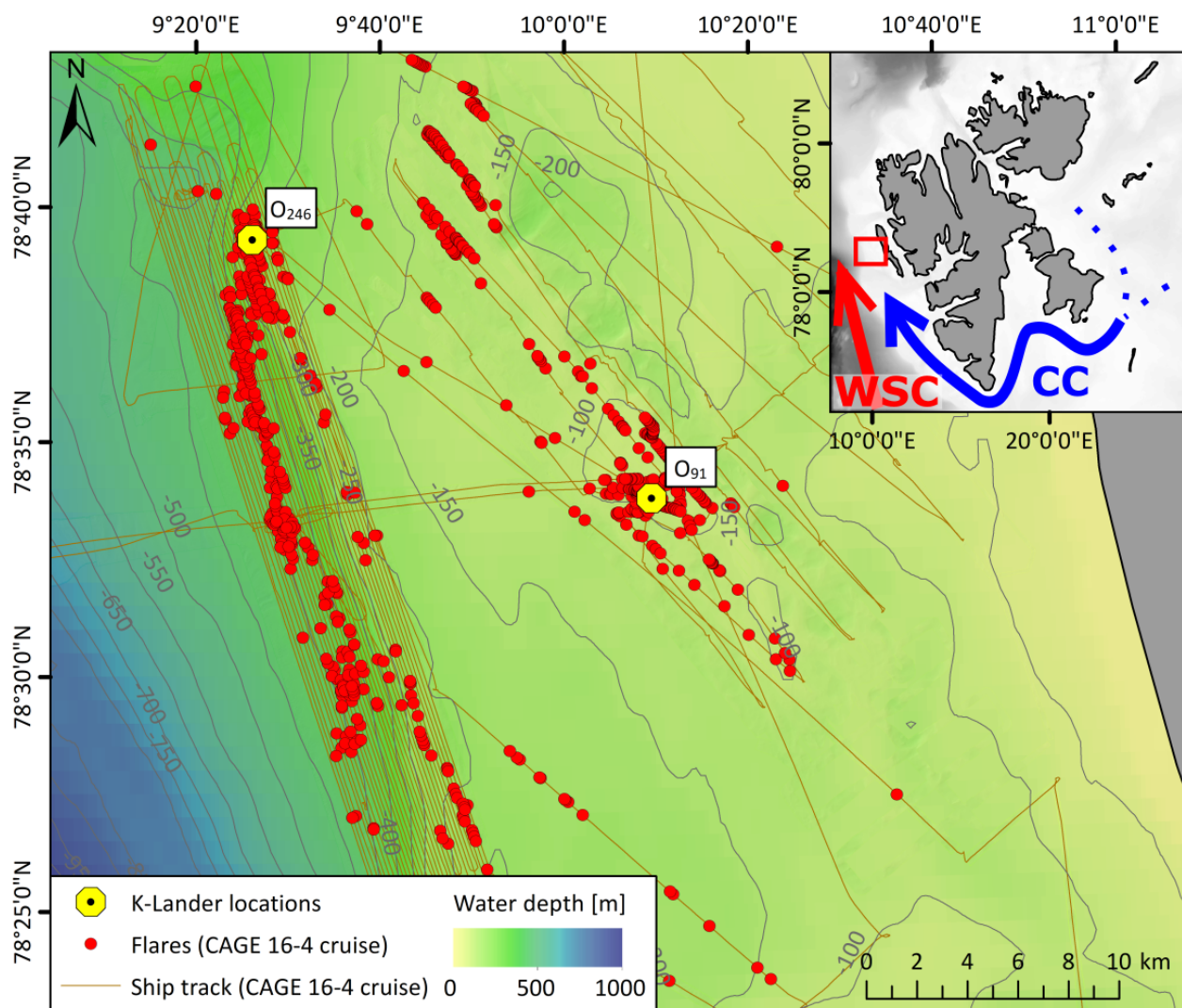
Figure 1. Bathymetry of the study area with location of the observatories O_{91} and O_{246} offshore western Svalbard. Flares detected by single-beam echo sounder survey prior to recovering the observatories (May 2016, cruise CAGE 16-4) are indicated with red dots and ship tracks as brown lines. The inset map shows the working area (red square) offshore Svalbard. WSC and CC refer to the warm West Spitsbergen Current and cold Coastal Current, respectively.

give an overview of linear relationships between the measured parameters. We mapped the flares in the area using single-beam echo-sounder data collected during the observatory recovery cruise in 2016 (CAGE 16-4, Figure 1) and estimated gas flow rates using the FlareHunter software (Veloso et al., 2015). Additionally, we obtained 10 m wind reanalysis data from the ERA-Interim database. Further description of general post-processing, technical features of the data and measurement accuracies are outlined in Appendix B and Table B1.

We calculated seawater density (McDougall and Barker, 2011) and CH_4 solubility (Kossel et al., 2013) using the CTD data. A CTD cast (SBE plus 24 Hz) prior to the O_{91} recovery (6 May, 2016) showed a salinity drift in the conductivity sensor of around -0.4. Post-calibration, inspection of the conductivity signal and potential water mass mixing end-members indicates that this might have been caused by mud pollution occurring in late 2015 or early 2016.

High power consumption of the Contros HydroC CH_4 and CO_2 sensors required a power cycling mode to allow for long-term monitoring while simultaneously capturing rapid short-term variability. Partial pressure of CH_4 and CO_2 was therefore measured continuously for 24 hours every 21 days, and for one hour every day (see Table B1). CH_4 concentration data were corrected for slow response time following Dølven et al., (In prep.) onto a 3 minute interval grid and converted to absolute concentration (see Appendix C), which is the default "CH_4 concentration" discussed and described in this text. Faulty pumps in the CO_2 sensors ambiguously increased the response time, preventing us from performing response time correction and making CO_2 data suitable only for long-term qualitative analysis.

3 Results

3.1 Time series at site O_{91}

Dissolved CH_4 concentration at site O_{91} ranged from 5 nmol L^{-1} (6 December in 2015) to 1 348 nmol L^{-1} (20 August in 2015) (Figure 2a) following a log-normal distribution, with a mean and median of 227 and 165 nmol L^{-1}, respectively. Large variations (>100 up to almost 1000 nmol L^{-1}) in CH_4 concentration occurred on short time-scales (<1 hour) throughout the measurement period (see Figure 2a, d, and all 24-hour periods in Appendix D) with an average range for all the 24-hour periods of 840 nmol L^{-1} and median rate of change (ROC) of 3.2 nmol L^{-1} min^{-1}. We also observe a long-term trend of decreasing running median (2-week window) concentrations towards winter, from 495 nmol L^{-1} in July/August 2015 to 53 nmol L^{-1} in January 2016 (Figure 2). There was a relatively weak, but significant negative correlation between the wind speed and CH_4 concentration (R_{RTC}=-0.33), but otherwise weak to non-existent linear relationships between CH_4 concentration and the measured ocean parameters (Table 1).

CO_2 averaged 403 μatm with a decrease from mid-November 2015 (~400 μatm) until 6 May (~391 μatm) in 2016 (Figure 2a). CO_2 dropped to ~305 μatm on 24 August, concurrent with a rapid decrease in salinity (-0.5), increase in temperature and oxygen, and high CH_4 concentration. The oxygen increase rules out methanogenesis. Instead, there might be at least two explanations for this reduction of CO_2 and enrichment of CH_4: i) water column mixing brings oxygen-rich, warm and fresh surface water to deeper depth, and with it CO_2 depleted water or ii) methane enrichment by zooplankton following the summer bloom.
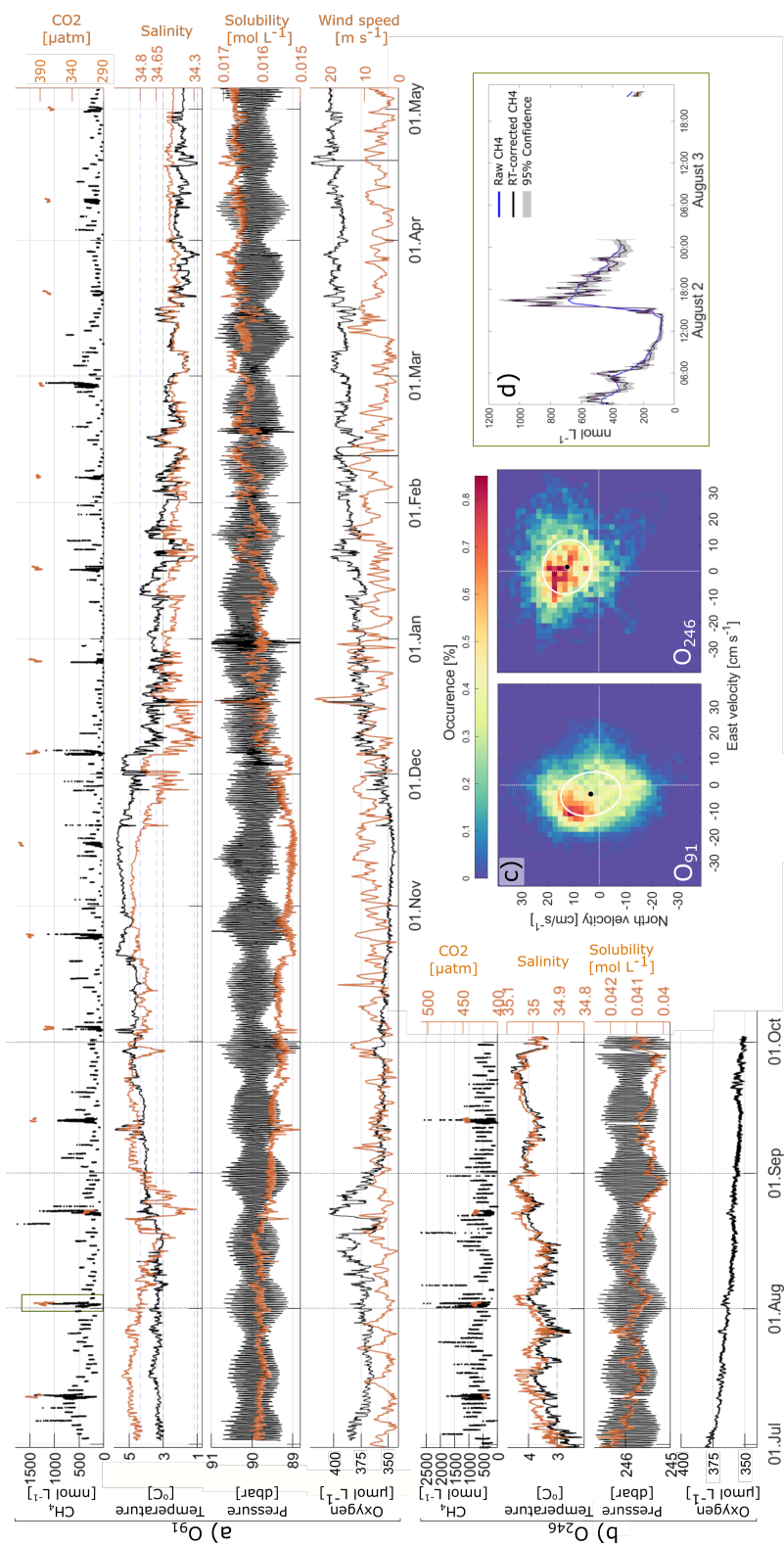
Figure 2. Time series from a) O_{91} and b) O_{246} showing response time corrected (see Appendix C) CH_4 and CO_2 concentration, temperature, salinity, pressure, CH_4 solubility, oxygen, wind speed (10 m). c) 2-d histogram and 1 standard deviation variance ellipse of bottom current velocity (81 m depth at O_{91} and 236 m depth at O_{246}) and d) example of 24-hour and 1-hour (2 and 3 August) CH_4 concentration measurement period from O_{91} (green box). All 24-hour measurement periods are shown in Appendix D.

Table 1. Correlation coefficients between variables at O_{91}. "RTC CH_4" and "Raw CH_4" refers to response time corrected and untreated CH_4 (see Appendix C). Units used are mol L^{-1}, ^oC, salinity, mol L^{-1}, dbar, mol L^{-1}, m s^{-1}, and μatm for dissolved CH_4, temperature, PSU, dissolved oxygen, pressure, CH_4 solubility, wind speed, and partial pressure of CO_2, respectively.

	RTC CH_4	Raw CH_4	Temperature	Salinity	Oxygen	Pressure	Solubility	Wind speed	CO_2
RTC CH_4	1	0.91	-0.06	0.23	0.03	0.08	0.06	-0.33	-0.25
Raw CH_4	0.91	1	-0.07	0.27	0.03	0.10	0.06	-0.37	-0.31
Temperature	-0.06	-0.07	1	0.69	-0.94	-0.01	-0.99	0.37	0.29
Salinity	0.23	0.27	0.69	1	-0.78	-0.06	-0.58	0.06	0.46
Oxygen	0.03	0.03	-0.94	-0.78	1	0.02	0.85	-0.33	-0.67
Pressure	0.08	0.10	-0.01	-0.06	0.02	1	0.16	0.00	-0.10
Solubility (CH_4)	0.06	0.06	-0.99	-0.58	0.85	0.16	1	-0.35	-0.30
Wind speed	-0.33	-0.37	0.37	0.06	-0.33	0.00	-0.35	1	0.52
CO_2	-0.25	-0.31	0.29	0.46	-0.67	-0.10	-0.30	0.52	1

Bottom water temperature increased steadily from $\sim$3 in July to $\sim$5.5 ^oC in October/November 2015, with occasional sharp shifts (T$\pm$1^oC) occurring within hours to days (Figure 2b). Temperature then decreased from the beginning of December to $\sim$1.8^oC at the end of the deployment in May 2016, showing more frequent and stronger episodes of rapid temperature shifts (T$\pm$2^oC also occurring on hours-days). Despite uncertainty in salinity data, it is worth noting that these rapid shifts in temperature and salinity was reproduced by the Svalbard 800 model in the same area (Silyakova et al., 2020) by eddy activity.

Hydrostatic pressure was mostly governed by tides (94.5% of variance) with dominant semi-diurnal M2 tide (M2 refers to a tidal constituent with period 12.42 hours, see e.g. Gerkema (2019)). Amplitudes varied from $\sim$1.2 to 1.5 meter during neap and spring cycles (Figure 2c).

The calculated CH_4 solubility decreased from 0.016 mol L^{-1} in July to 0.015 mol L^{-1} in the end of November 2015, and increased to almost 0.017 mol L^{-1} in May 2016 (Figure 2c). This long-term trend was mainly caused by temperature variability (R=-0.99), while tidal pressure changes caused a semi-diurnal variation of $\pm$ $\sim$0.005 mol kg^{-1}.

Dissolved O_2 decreased from $\sim$385 μmol L^{-1} in July 2015 to $\sim$350 μmol L^{-1} at the beginning of December, and increased to $\sim$400 μmol L^{-1} towards 6 May, 2016 (Figure 2d) and followed temperature inversely (R=-0.94), with similar long and short-term variability.

The averaged bottom water current (81 m above the seafloor) was 4 cm s^{-1} in a northwestward direction (321°N) (Figure 2c). The current usually had one anti-clockwise rotation every 23.93 hour period, corresponding to the diurnal K1 tidal constituent (tide with period 23.93 hours, see Gerkema (2019)) with a secondary semi-diurnal (M2) modulation.

3.2 Time series at site O_{246}

CH_4 concentration at site O_{246} ranged from 10 nmol L^{-1} on 21 September, 2015 to 2727 nmol L^{-1} on 18 August 2015,
140 following a log-normal distribution with an average and median of 577 and 600 nmol L^{-1}. The median RoC of CH_4 was
almost 20 times higher compared to site O_{91} with 31 nmol L^{-1} min^{-1} (Figure 2b and Appendix D). There was also clear
diurnal periodicity in CH_4 concentration at O_{246}. The long-term trend (2-week running mean) shows decreasing concentrations
until 3 October 2015 (end of the measuring period, Figure 2b). Dissolved O_2 decreased from $\sim$380 μmol L^{-1} to $\sim$300 μmol
L^{-1} and was negatively correlated with water temperature (R=-0.61, see Table 2 for complete correlation matrix).

Table 2. Correlation coefficients between variables at O_{91}. "RTC CH_4" and "Raw CH_4" refers to response time corrected and untreated CH_4
(see Appendix C). Units used are mol L^{-1}, ^oC, salinity, mol L^{-1}, dbar, mol L^{-1}, m s^{-1}, and μatm for dissolved CH_4, temperature, PSU,
dissolved oxygen, pressure, CH_4 solubility, wind speed, and partial pressure of CO_2, respectively.

	RTC CH_4	Raw CH_4	Temperature	Salinity	Oxygen	Pressure	Solubility	Wind speed	CO_2
RTC CH_4	1	0.78	-0.31	-0.24	0.30	0.15	0.33	-0.29	-0.13
Raw CH_4	0.78	1	-0.45	0.26	0.48	0.10	0.45	-0.44	-0.09
Temperature	-0.31	-0.45	1	0.87	-0.61	-0.02	-0.99	0.38	0.22
Salinity	-0.24	-0.26	0.87	1	-0.22	-0.03	-0.87	0.07	0.13
Oxygen	0.30	0.48	-0.61	-0.22	1	0.06	0.59	-0.65	-0.41
Pressure	0.15	0.01	-0.02	-0.03	0.06	1	0.16	-0.05	0.14
Solu (CH_4)	0.33	0.45	-0.99	-0.87	0.59	0.16	1	0.38	-0.20
Wind speed	-0.29	-0.44	0.38	0.07	-0.65	-0.05	0.38	1	0.18
CO_2	-0.13	-0.09	0.22	0.13	-0.41	0.14	-0.20	0.41	1

145 Temperature and salinity increased from $\sim$2.5 to $\sim$4.0 ^oC and $\sim$34.85 up to $\sim$ 35.0, respectively, from the deployment
until October 2015 (Figure 2b), with AW dominance throughout the measuring period. Rapid shifts of around $\pm1^oC$ and 0.05
salinity occurred occasionally over a period of hours to days.

Variance in hydrostatic pressure was mainly explained by the tides (95.2%) which was mainly governed by the semi-diurnal
M2 tide, with weaker diurnal and fortnightly modulation (Figure 2b). Changes in pressure varied from $\sim$1.2 to $\sim$1.5 m during
150 periods of neap and spring tide.

Being governed mainly by temperature (R=-0.99), CH_4 solubility dropped from 0.042 mol L^{-1} to 0.040 mol L^{-1} from the
deployment in July until October 2015, with a semi-diurnal variation of $\sim$0.005 mol L^{-1} due to tidal changes in hydrostatic
pressure.

The averaged current was $\sim$ 10 cm s^{-1} northward (7^oN) (Figure 2c). Variability in the along-slope current (direction -10^oN)
155 was strongly related to the semi-diurnal M2 tidal component, while the cross-slope currents were governed by the diurnal
K1 frequency. The bottom water current rotated counter-clockwise with a period of 23.93 hours (K1 tidal constituent), with
semi-diurnal modulation in the along-slope component. Dissolved CH_4 concentration was weakly anti-correlated with wind

speed (R=-0.29), temperature (R=-0.31), salinity (R=-0.24), and positively correlated with CH_4 solubility (R=0.33) and oxygen (R=0.3).

4 Discussion

4.1 CH_4 variability

Combining mapped flares and flow rates from the recovery cruise (May 2016) with bottom water current velocity (9 meters above the seafloor) reveals that CH_4 concentration was strongly affected by whether water was advected from areas where we mapped strong or weak seepage in May 2016 (Figure 3). Strong seeps (flow rate >200 mL^{-1} min^{-1}) were mainly located between $\sim$30 and 80 m to the north/northeast of site O_{91} and only weak and more distant seepage was observed south-west of the observatory (Figure 3a). Consequently, averaged CH_4 concentration from water coming from north-east was $\sim$440 nmol L^{-1}, while water from south-west averaged $\sim$100 nmol L^{-1}. Similarly, a strong CH_4 seep (flow rate $\sim$1200 mL min^{-1}) was mapped $\sim$40 m north of site O_{246}, making water advected from this direction highly elevated in CH_4 with an average of $\sim$1400 nmol L^{-1} compared to the overall average of 577 nmol L^{-1} (Figure 3b). The rapid changes in dissolved CH_4 can to a high degree be explained by this relationship, due to the high variability in ocean current velocity. That this relationship holds for most of the measuring period also shows that seepage and seep configuration did not change significantly from July 2015 to May 2016 (no winter season seep hibernation as observed in Ferré et al. (2020)) and that dissolved CH_4 was efficiently dispersed in high concentrations in the whole seepage area.

Furthermore, daily CH_4 concentrations at site O_{91} were higher on average than the 24-hour measurements (313 vs. 200 nmolL^{-1}). This can explained by the comparable measurement periodicity (24 hours) and tidal periodicity (23.93 hours) in the ocean currents, resulting in predominantly eastward advection during daily measurements, thus systematically transferring more water from a weak seepage area (Figure 3). We did not observe this effect at site O_{246}, most likely due to less tidal variance in the current direction (Figure 2b). Nonetheless, this systematic tide induced bias on the daily measurements at site O_{91} highlights the importance of taking the oceanographic conditions into account to avoid misinterpretation of variability.

Since currents are mostly northward and seepage are mostly located to the north of both observatories, averaged CH_4 concentrations are also most likely lower than the average over the immediate surrounding area (Figure 3). Despite this, the observatory data show higher average CH_4 concentrations than previously reported. In the area surrounding site O_{91}, Silyakova et al., (2020) reported average concentration of 92, 70, and 61 nmol L^{-1} in June 2014, July 2015, and May 2016, respectively, based on discrete water sampling. Averaged CH_4 concentrations measured at site O_{91} in July 2015 and May 2016 were 566 and 110 nmol L^{-1} respectively, i.e. around eight and two times higher than values reported by Silyakova et al., (2020). The maximum CH_4 concentration at O_{91} of 1789 nmol L^{-1} on 20 August 2015 also significantly exceeds the previously maximum recorded concentration in the area of 480 nmol L^{-1} (July 2014, Silyakova et al., 2020).

At site O_{246} the August 2016 average (564 nmol L^{-1}) was eight times higher than what Gentz et al., (2014) found in August 2010 (70 nmol L^{-1}), using an altimeter-controlled CTD towed at 2 meter above the seafloor. Maximum concentration
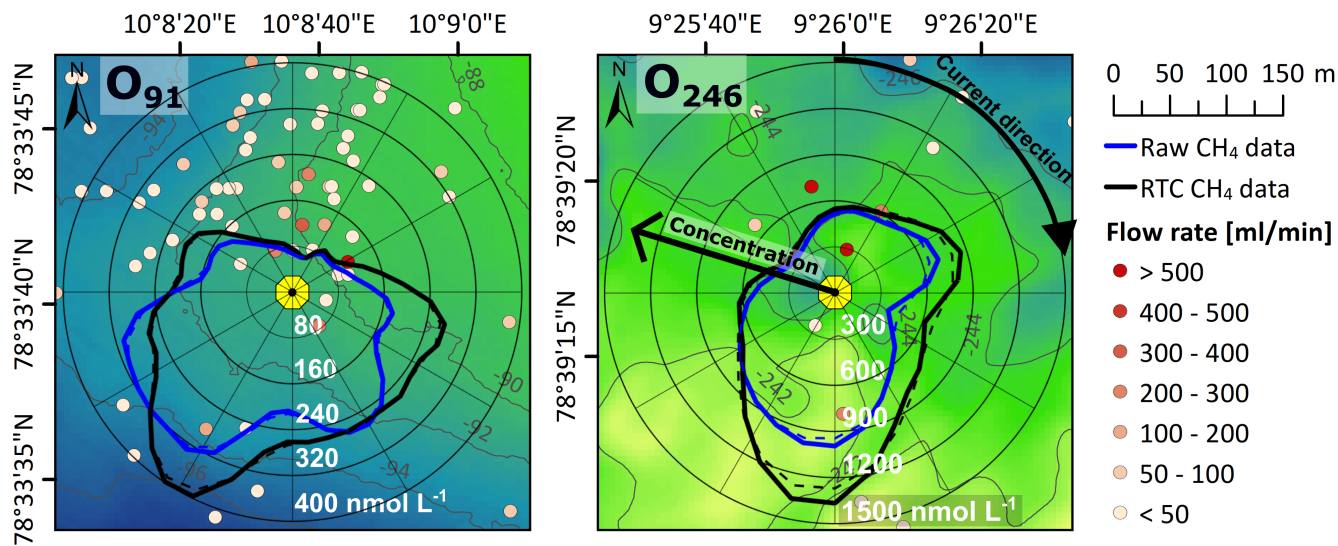
Figure 3. O_{91} (left) and O_{246} (right) location (yellow dot) as well as flow rates from flares mapped in its vicinity during CAGE 16-4 (colorscale). Background color (grene-blue) illustrate seafloor bathymetry. Compass diagram show the relationship between ocean current direction (angle) and CH_4 concentration (distance from center, black is response time corrected (RTC) data and raw data is in blue).

190   in August 2016 also significantly exceeded previous observations, with 2661 nmol L^{-1} compared to 524 nmol L^{-1} measured by Gentz et al., (2014).

     These differences could be a result of temporal, local or regional differences in CH_4 concentration. However, strong vertical gradients in dissolved CH_4 are well documented at both seep sites (Gentz et al., 2014), and our sensors measured closer to the seafloor (1.2 m above seafloor), compared to Gentz et al., (2014) (2 m above seafloor) and Silyakova et al., (2020) (5 to 15

195 m above seafloor). Additionally, the observatories were deployed close to seeps using a launcher as opposed to "blind" water sampling from ship-born rosette. Methane was also measured in situ, thereby avoiding potential CH_4 outgassing after retrieval of water samples (Schlüter et al., 1998).

     We documented high local variability, steep concentration gradients, strong connection to highly variable ocean currents and higher CH_4 concentrations than previously reported in the same areas. Dissolved CH_4 within shallow seep sites where

200 the gas can bypass the oceanic sinks often present heterogeneous distribution and rapid temporal variability (Myhre et al., 2016a; Mau et al., 2017; Veloso-Alarcón et al., 2019). Our results show that the variability in space and time at our two seep sites are higher and faster than previously reported, at least in bottom water (<2 m above the seafloor). This underlines an important caveat when using snap-shot surveys and interpolation/extrapolation techniques to estimate CH_4 inventories and fluxes. As shown herein, CH_4 concentration at our locations can change by up to 2 orders of magnitude within hours

205 (Figure 2d), while ship-based "snapshot" surveys often take place over several days. Using ship based discrete water sampling and interpolation/extrapolation techniques which assumes an even/linear distribution when the distribution of CH_4 is in fact patchy, may well explain discrepancies between top-down and bottom-up approaches to estimate CH_4 inventories in, and

fluxes from the ocean (e.g. discrepancies between Shakhova et al., (2010) and Berchet et al., (2016)). It is also important to acknowledge that ocean currents are often periodic and to a certain degree systematic in their behavior, implying potential

210 systematic measurement errors.

Our findings highlight the advantage of towed or autonomous instrumentation capable of providing continuous CH_4 data giving a considerably better coverage and representation of the CH_4 distribution in a much shorter time frame (e.g. Sommer et al., (2015) and Canning et al., (2021)). They also stress the importance of having a systematic grid when collecting water samples for inventory estimates in intense seep areas, thereby allowing the law of large numbers to apply. Assuming a lognor-

215 mal distribution, which better reflects the uneven spread of CH_4, when applying interpolation/extrapolation techniques could further limit estimation errors. It also shows the importance of getting a good overview of the ocean currents and location of CH_4 seeps to mitigate uncertainties in sparsely sampled areas to avoid potential systematic errors.

4.2 Hydrostatic pressure

Tidal changes in hydrostatic pressure can trigger CH_4 release by build-up of CH_4 in sediment pore-water at rising tide and

220 subsequent release when pore pressure decreases at falling tide as observed at the Hikurangi Margin (Linke et al., 2009) and Clayoquot slope (Römer et al., 2016). Our study sites differs from these sites in depth (they are >600 m) and in tidal amplitude (4 m at Calyoquot slope compared to 1.5 at PKF). Linke et al., (2010) and Römer et al., (2016) also observed bubbles hydro-acoustically, while we measure dissolved CH_4 which is strongly affected by the (also tidally dependent) current direction (Figure 3).

225 To constrain this effect on CH_4 concentration, we separated the data into overlapping portions depending on the current direction (12° and 30° for O_{91} and O_{246}, respectively) and calculated standard scores of CH_4 concentration for each portion which are less dependent on current direction. We used larger current direction intervals for O_{246} due to the shorter data set. We then binned all the z-scored CH_4 data according to when the data were collected in relation to the M2 governed tidal cycle peak using overlapping 30 minute bins (the M2 tide explains 79.2% and 80.3% of the pressure variance at O_{91} and O_{246},

230 respectively). Average and median values were then calculated for each bin, giving the averaged/median normalized dissolved CH_4 value (standard score) for each current velocity defined data portion as a function of the M2 tidal cycle (Figure 4). This partial decoupling of variability in hydrostatic pressure and current direction was possible since the bottom water current and hydrostatic pressure changes had different dominant tidal constituents, i.e. the current was mainly dominated by the diurnal K1 constituent (~23.91 hour period), while the M2 tide is semi-diurnal (12.42 hour period).

235 A strong effect of the hydrostatic pressure on local seepage should elevate z-scores at decreasing pressure (from 0 to 6.2 hours, i.e. in the right half of Figure 4), which we observe at both observatories. However, we observe stronger peaks at increasing hydrostatic pressure (-3 hours) at site O_{91} and at the M2 peak (0 hours) at site O_{246}, which contradicts this hypothesis. This does not mean that there is no effect of hydrostatic pressure changes, but rather that the seepage in the area is widespread at both falling and rising tide conditions. The high variability caused by the strong effect of current direction also makes it

240 particularly challenging to detect moderate changes in seepage intensity.
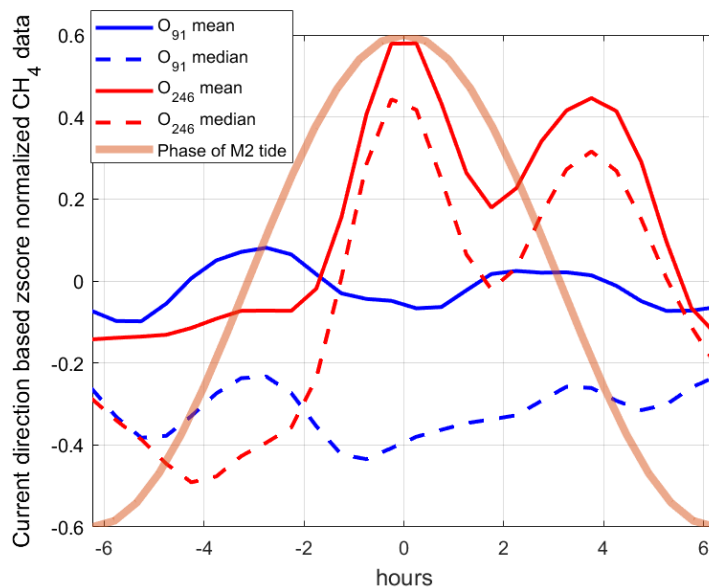
Figure 4. Median and averaged z-scores of CH_4 binned according to bottom water current direction according to where the data were sampled on the phase of the M2 pressure tide.

4.3 Bottom water temperature

Bottom water temperature can affect CH_4 release by altering hydrate stability and CH_4 solubility in pore water and water column (Sloan, 1998; Jansson et al., 2019a). Seasonal CH_4 release variability resulting from temperature variations in the bottom water has been linked to migration of the GHSZ and hydrate dissociation further offshore at ~ 390 m water depth (Berndt et al., 2014; Ferré et al., 2020). Our observatories were deployed in areas too shallow for gas hydrate to form. However, inversely varying seepage intensity between seepage at the GHSZ depth (390 m) and site O_{246} can suggest that these areas are fed by the same hydrocarbon source and that hydrates seasonally block the lateral pathways between these seep sites (Veloso-Alarcón et al., 2019). This is in agreement with the observed long-term (~ 3 months) negative correlation between bottom water temperature and dissolved CH_4 at site O_{246} (R=-0.31). It should be noted that the same relationship is observed at O_{91}, however no geophysical data are available from this area due to the shallow depth.

Tidal pressure variations can affect CH_4 release via pore water solubility (Sect. 4.2), but on longer timescales, CH_4 solubility is almost exclusively a function of water temperature. Higher CH_4 solubility implies more CH_4 dissolved in pore water and within bubble streams, potentially increasing the amount of CH_4 dissolved in bottom water. A small but significant (R=0.33) positive correlation between CH_4 solubility and concentration at site O_{246}, and site O_{91} (considering the same time period, i.e. until 3 October in 2015), could indicate such an effect. This is also an alternative explanation for the negative correlation between temperature and CH_4 concentration at site O_{246}.

4.4 Pore water seepage

Short-term temperature increase further offshore (390 m depth) has been linked with release of warm, CH_4 rich fluids from
the sediments triggered by short duration seismic events (Franek et al., 2017). This means that increased CH_4 concentration

260 should be accompanied by increased water temperature and reduced salinity due to admixture of warmer, less saline pore
water. We compared short-term anomalies (i.e., deviations from daily means) in these three variables in the 24-hour data sets at
both seep sites, but found no corroborating evidence for this hypothesis. Instead, the covariance between current velocity and
temperature and salinity anomalies indicates that short-term variability is mainly caused by cross-shelf exchange of AW in the
WSC and ArW in the CC due to eddies (Hattermann et al., 2016). It also indicates that CH_4 release comes mainly from bubble

265 dissolution and not pore water seepage.

4.5 Seasonal variation of CH_4 distribution at site O_{91}

Low atmospheric release of CH_4 from O_{91} during summer, despite high seabed influx, has been explained by suppression of
vertical mixing by strong stratification (Myhre et al., 2016a) or absence of mechanical forcing such as wind stress (Silyakova
et al., 2020). However, in fall and winter, the water column offshore PKF is expected to have more horizontal and vertical

270 mixing due to weaker stratification from cooling or sea ice formation (Tverberg et al., 2014), baroclinic instability in the
frontal structures of the WSC (von Appen et al., 2016; Hattermann et al., 2016), and more frequent storms (Nilsen et al., 2016).

We expect lower CH_4 variability and lower CH_4 concentration during periods of high mixing and dispersion, due to weaker
horizontal and vertical gradients and more efficient dispersion of CH_4 away from sources. We use three sets of parameters
to evaluate long term changes in the amount of mixing in the water column (see Appendix E): i) the 4-week averaged bulk

275 velocity shear (S_b), ii) the two dimensional correlation between wind stress and current velocity (R_{WC}), and iii) the number
of stormy days defined by persistent winds >11 m/s lasting longer than 6 hours (Figure 5). Calm weather, low S_b and R_{WC}
until mid-September 2015 indicate a stable water column with limited mixing in the bottom waters. From mid-September, S_b
increased and stayed high until mid-November, together with a gradual increase in R_{WC} which can be attributed to a gradual
breakdown of stratification and increasing number of storm events (Figure 5a). R_{WC} remained high (R_{WC} >0.5 at 60 m depth)

280 until March 2016, indicating significant effect of wind forcing in the water column. From March until observatory retrieval,
R_{WC} decreased to < 0.2 below 50 m depth while S_b increased below 60 m depth, indicating available energy for mixing in the
bottom waters.

We quantified CH_4 variability during the 24-hour measurements using the Median Absolute Deviation (MAD) and used
the median as a measure of the amount of dissolved CH_4. The three 24-hour periods collected during the calmer period prior

285 to mid-September had high median concentration (>300 nmol L−1) and the overall highest variability (MAD>160 nmol
L−1), as expected for low mixing conditions (Figures 5b and 5c). From mid-September until the end of March (i.e. fall/winter
season), the 24-hour CH_4 concentration time-series had generally lower MAD and median concentration. In this period, CH_4
variability and median also showed a good statistical relationship with the 5 days accumulated wind stress (R=-0.82 for MAD
and R=-0.61 for median concentration), indicating that wind forcing has a deep impact on mixing and redistribution of CH_4
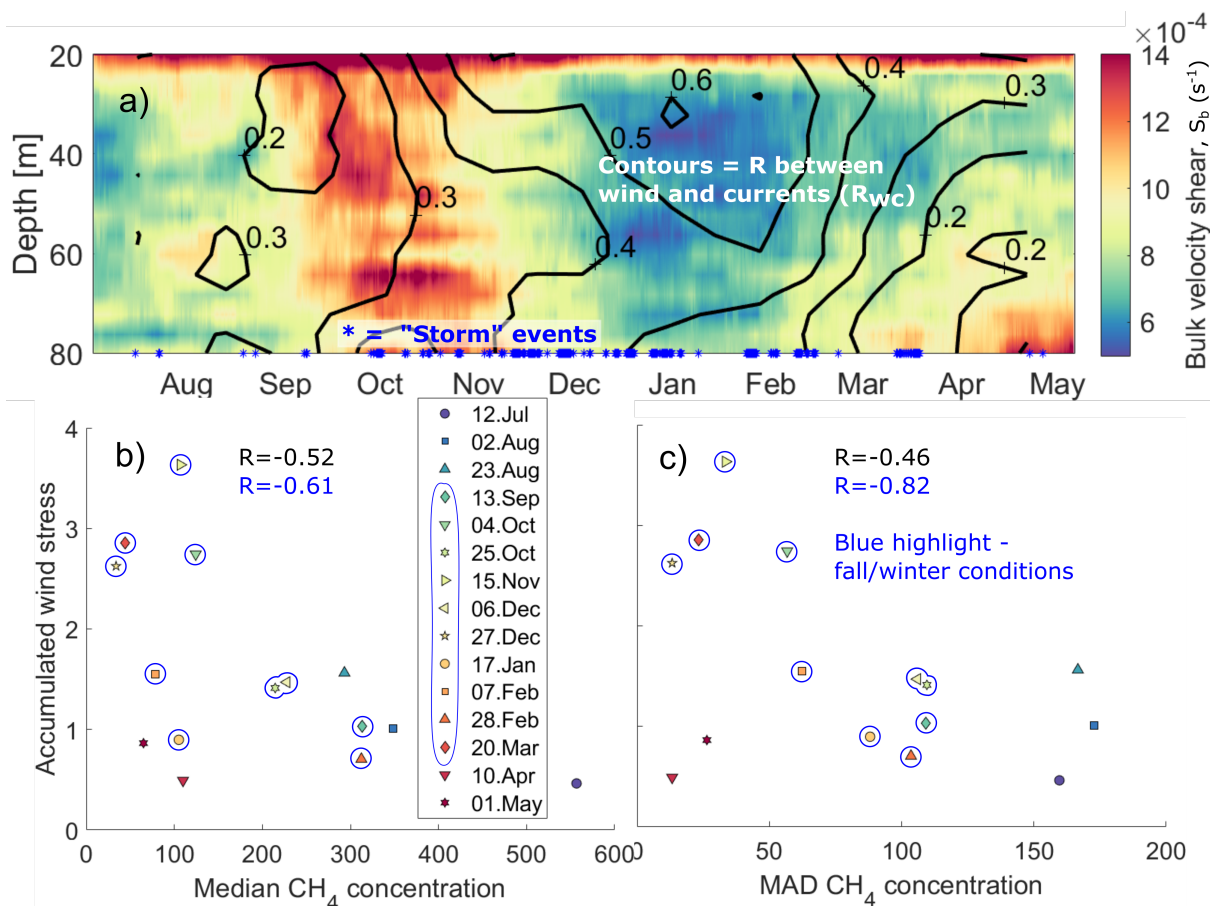
Figure 5. a) Bulk velocity shear (ΔH = 8 meter) and two dimensional correlation with wind stress (contours). Relationship between 5 days accumulated wind stress and median (b) as well as median absolute deviation (c) of CH_4 concentration for 24 hour data periods. Persistent wind events with more than 10 m s^{-1} winds in periods over 6 hours are indicated with blue stars along the x-axis of diagram a). Blue highlights fall/winter water column conditions as described in the text.

290 in the water column (which also fits well with a high R_{WC}). The two last 24-hour CH_4 time series (10 April and 1 May) had low median concentration, which could be explained by the absence of stratification (Silyakova et al., 2020) and generation of mixing from the observed increase in S_b.

Accumulated wind stress, S_b and R_{WC} are only limited indicators on water column dispersion and mixing. Nonetheless, the relationship between these parameters and the MAD and medians of the 24 hour period CH_4 time series gives a good indication

295 on the seasonal cycle of distribution and vertical transport of CH_4: strong stratification, less wind forcing and eddy activity in summer limits mixing and prevents CH_4 from reaching the atmosphere. However, in fall and winter, reduced stratification makes the water column more prone to mixing and distribution of CH_4 seems to be strongly linked with wind forcing from September to April.

5 Conclusions

Time-series of dissolved CH_4 at both lander locations show considerably higher CH_4 concentrations (up to 1789 nmol L^{-1} at O_{91} and 2727 nmol L^{-1} at O_{246}) than previously estimated from ship-based water sampling surveys (maximum of 482 near O_{91} and of 564 near O_{246}). The time-series also uncover high CH_4 variability (up to $\sim$1000 nmol L^{-1}) within short timescales (< 24 hours) and a heterogeneous CH_4 distribution, highlighting the uncertainty of flux/inventory estimates based on interpolation/extrapolation techniques where even/linear CH_4 distribution is assumed. Variability can be linked to directional ocean current variations occurring at tidal time-scales which shows the importance of taking the current direction and seep locations into account when interpreting intense seep site observations. The persistent relationship between current direction and seep configuration shows that there is no significant change in seepage through the year.

We did not observed a direct effect of tidal pressure variations on CH_4 release, but this could be hidden by the strong effect of variations in current direction. A negative (long-term) correlation between temperature and dissolved CH_4 at O_{246} is in agreement with the hypothesized seasonal blocking of lateral CH_4 pathways in the sediments (Veloso-Alarcón et al., 2019) but could also be explained by increased CH_4 solubility in the water column.

Short-term, small-scale variations in temperature and salinity were not linked with increased amounts of dissolved CH_4, but rather with cross-frontal exchange of water masses due to eddies.

We observed a seasonal cycle in the characteristics of the 24-hour time-series which fits with seasonal changes in dispersion and mixing characteristics of the water column. Higher CH_4 concentration and variability in early fall, when stratification was strong, was followed by lower median concentrations and variability in late fall/winter when the water column was more affected by mixing. In late fall/winter, wind forcing was statistically coupled to the concentration and variability of CH_4, probably due to weaker water column stratification.

When estimating the atmospheric impact of a particular CH_4 source based on sparse measurements, it is crucial to have some constraint on the temporal and spatial variability. These constraints can either be direct knowledge about variability itself or how inventory and fluxes are affected by related physical and/or chemical parameters. We observed considerable temporal and spatial variability at the two seep sites which need to be taken into account to obtain meaningful estimates of CH_4 fluxes or inventories. That no strong direct link was found with other oceanographic parameters illustrate the non-linearity of the system, making careful interpretation of measurements important. Based on our observations, we suggest that uncertainties in CH_4 inventory and seep estimates can be mitigated by taking the local seep configuration, ocean currents and mixing rates into account, avoid linear interpolation techniques (or using more suitable distribution assumptions), and employ autonomous instrumentation capable of resolving the steep horizontal gradients in dissolved CH_4. This, alongside direct measurements of seepage by e.g., acoustic instrumentation, can help constrain future estimates of CH_4 flux to the atmosphere from seabed seepage.

330 *Code and data availability.* All data presented in this paper can be obtained upon request to the authors and will also be made available in the platform Open research Data at the University of Tromsø – The Arctic University of Norway (https://dataverse.no/dataverse/uit). All computer code being used can be obtained upon request to the corresponding author

Appendix A: The K-Lander
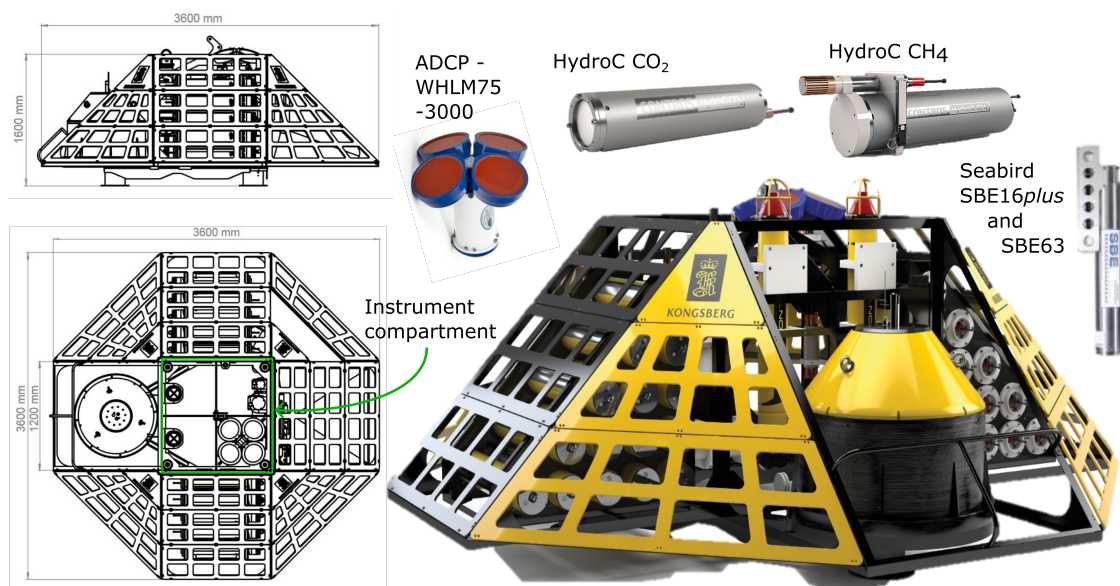
Figure A1. The K-Lander is a 1.6 m high and 3.6 m wide trawl-proof stainless-steel frame with multiple instrument mounts and batteries. Side panels are perforated to allow unobstructed water flow to the instruments inside the structure. See Appendix B for details on instrumentation.
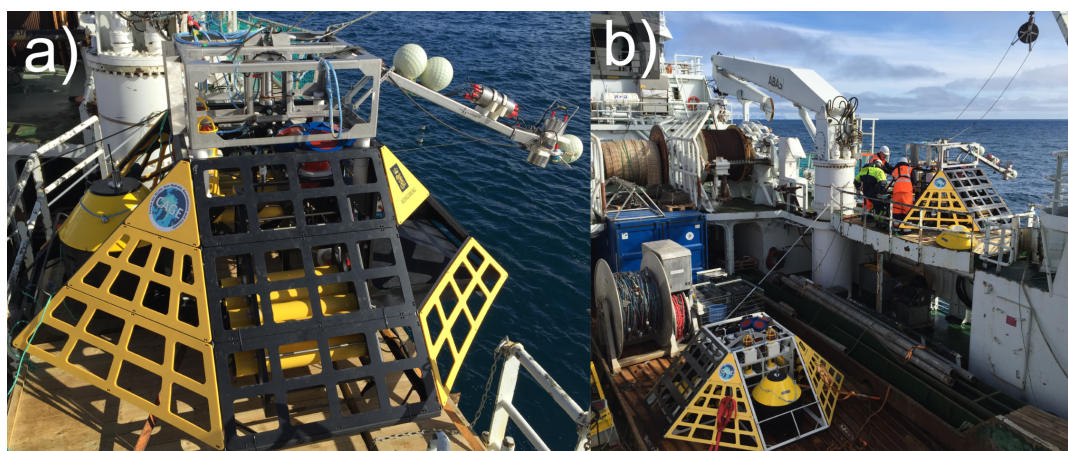
Figure A2. a) K-Lander during deployment with launcher mounted on top and camera system mounted on a boom for visual control of landing area. b) The two K-landers before deployment.

Appendix B: Measurement intervals, general post-processing and data

335 The CTD/oxygen sensor and ADCP conducted measurements every 4 and 9 minutes, respectively, during the continuous monitoring of CH_4 and CO_2 measurements, and 21 and 29 minutes during the rest of the deployment period (see Table B1 for acronyms, description, and measurement accuracy). Salinity was measured on the practical salinity scale.

The upward mounted ADCP measured ocean currents in 1 m bins with a bottom 7 m blank distance, where the topmost 20% of the water column was disregarded due to side lobe interference. The high resolution, relatively short ensemble time (1 minute), and potential presence of CH_4 bubbles in the water resulted in noisy data. We dampened the noise by first removing any data points with error velocities exceeding one short-term (1 week) standard deviation, smoothed the data using a second order Butterworth low-pass filter with a 3-hour cutoff period and a spatial (i.e. vertical) moving average filter with a 5 m Hann window (increasing the blank distance to 10 meter). The accuracy of the ADCP data is therefore not explicitly constrained and is based on comparing current velocity frequency spectra before and after filtering, combined with averaged error velocity of 345 the raw data (Table B1).

Table B1. Instruments mounted on O_{91} and O_{246} (see Figure A1), measured parameters, height in meters above sea floor (masf) and stated accuracy. ADCP stands for Acoustic Doppler Current Profiler. N shows the number of data-points used for later multi-variable analysis for O_{91}/O_{246}. (*)The Contros HydroC CH_4 output partial pressure from the internal gas chamber. (**)We report absolute concentration in seawater (nmol L^{-1}) using Henry's law and (***) report accuracy only for response time corrected (RTC) concentration (see Appendix C) since the accuracy for untreated CH_4 concentration data is ambiguous due to the slow response time.

Instrument	Parameter(s)	masf	N	Accuracy
Teledyne RDI ADCP WHLM75-3000	Current velocity Profile	1.6	17438/4731	$\sim$3 cm s^{-1}
Contros HydroC CH_4	pCH_4 (instrument output)* xCH_4 (reported**)	1.2	1491/281	$\sim$5-20%(RTC***)
Contros HydroC CO_2	pCO_2	1.2	1491/281	N/A (no pump)
SeaBird SBE16*plus* V2	Conductivity/Temperature /Depth	1.2	29660/9065	0.0005Sm^{-1}/0.005^{o}C, /0.02% of range
Seabird SBE63 oxygen optode	Dissolved Oxygen	1.2	29660/9065	3μmol kg^{-1} or $\pm$2%

Since sensors were recording at different frequencies, chronological alignment of the data was carried out by identifying nearest neighbor data points or by resampling. For correlation coefficients, histograms, and Fourier analysis, the data sets were resampled to a uniform 15 minute or 1 hour measuring interval depending on the sample frequency of the raw data, using a poly-phase anti-aliasing filter. Due to the power-cycling mode of the CH_4 and CO_2 sensors and differing sampling frequencies, 350 some statistics were based on more data points than others (outlined in Table B1). Daily measurements of CH_4 were excluded from statistics due to the high probability of systematic errors induced by periodic diurnal effects.

Harmonic analysis of hydrostatic pressure and ocean currents was done using t_tide (see Pawlowicz et al., 2002) and the fast Fourier transform.

We calculated the rate of change (ROC) in CH_4 concentration using the response time corrected CH_4 data and the absolute
355 value of the three point (9 minutes) finite differences to limit the effect of noise on the calculation.

The absolute concentration of CH_4 in the water (nmol L^{-1}) was estimated from the partial pressure of CH_4, pressure, temperature, and salinity, using Henry's law and Henry constants obtained from Harvey et al., (1996) and practical molar volume and gamma term from Duan & Mao et al., (2006).

Appendix C: Response time correction

360   In the Contros HydroC CH_4 and CO_2 sensors, dissolved gases diffuse through a hydrophobic membrane into a gas chamber
and equilibrate with the ambient environment. This results in a slow response time and poor representation of the rapid changes
in CH_4 as we expected in our study area (Gentz et al., (2013) and Myhre et al., (2016)). We therefore performed a response
time correction of the dissolved CH_4 data following the methodology presented in Dølven et al. (In prep) Briefly, this method
deconvolves slow sensor response using statistical inverse theory assuming that changes occur with time-step Δt, determined
365   based on domain-specific knowledge or L-curve analysis. The CO_2 sensors had a faulty pump, which ambiguously increased
the response time of the sensors making response time correction impossible.

The response time correction was performed for each period individually (1 hour and 24 hour, i.e. 377 periods), using the
stated measurement accuracy of the instrument (2 μAtm or 3% of measured value, whichever is higher) as input uncertainty.
We first identified the ideal Δ t according to the maximum curvature point in the L-curves of the 24 hour measurement periods.
370   These varied slightly between each measurement period, but averaging close to 180 s (176.4 s). To keep the same measuring
interval for all the CH_4 data, we therefore corrected all the data with a specified Δ t of 180 s, which falls well within the bend
of the L-curve and should therefore safeguard a good balance between noise and model error (Figure C1). The uncertainty
estimate varied depending on the amount of CH_4 measured by the laser spectrometry in the measurement chamber of the
instrument and ranged from 4 to 80 nmol L^{-1} (95% confidence, high for high concentrations in measurement chamber and
375   vice versa) or $\sim$5-20% of response time corrected value.
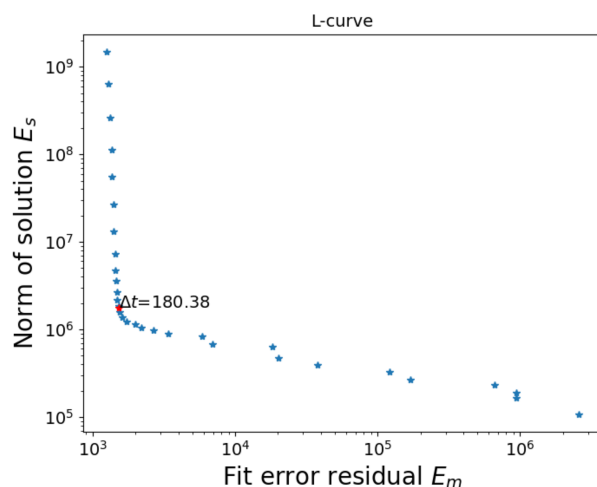
Figure C1. L-curve for response time correction of CH_4 data showing the location of the chosen Δt (180 s) for 6 May at O91.

Appendix D: 24-hour measurements of CH$_4$
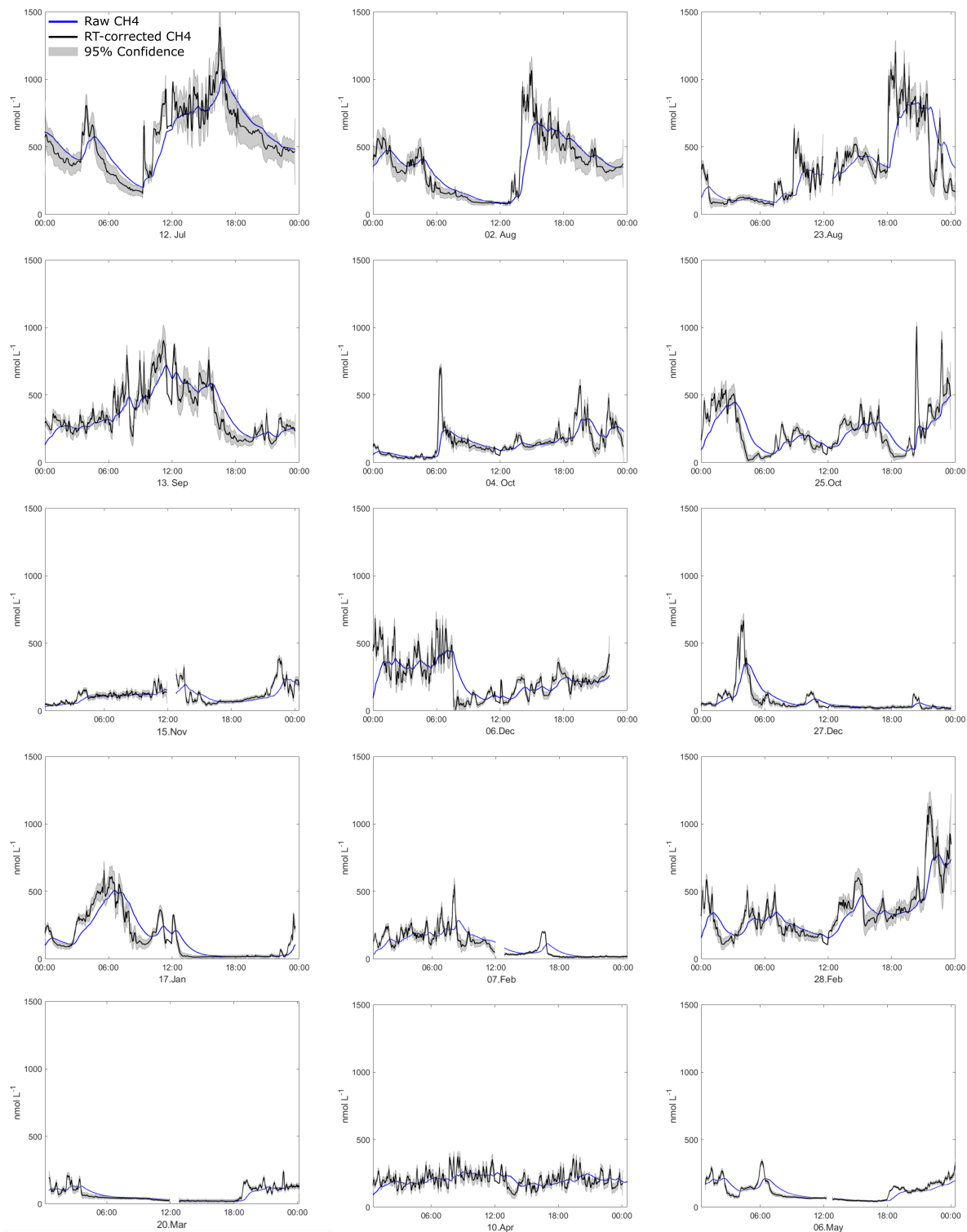
Figure D1. All 24 hour periods of CH_4 concentration at O_{91} with response time corrected data (black) with uncertainty estimate (grey shade, 95% confidence) and raw data (blue) from O_{91}.
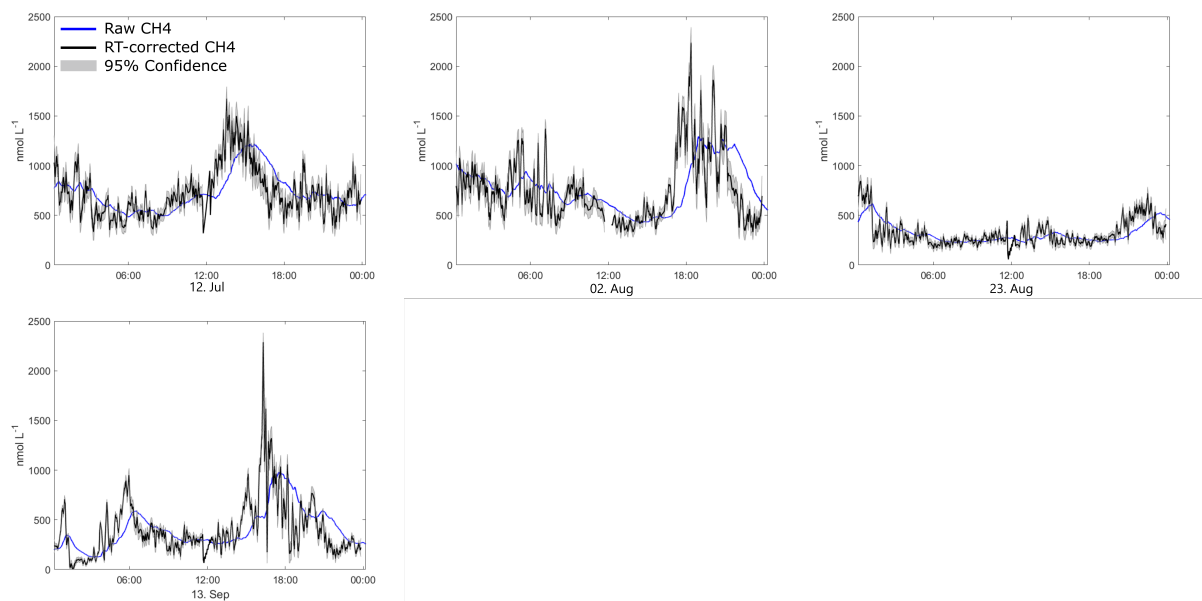
Figure D2. All 24 hour periods of CH_4 concentration at O_{246} with response time corrected data (black) with uncertainty estimate (grey shade, 95% confidence) and raw data (blue) from O_{246}.

Appendix E: Bulk velocity shear and wind stress correlation

We calculated bulk wind stress using 10 meter above sea level ERA-interim re-analysis wind data (Dee et al., 2011) and Large & Pond (1981). Water column bulk velocity shear S_b (see e.g. Lincoln et al., 2016) was calculated as

380
$$S_b^2 = \left(\frac{u_u - u_l}{h_{diff}}\right)^2 + \left(\frac{v_u - v_l}{h_{diff}}\right)^2 \tag{E1}$$

where u_u, u_l, v_u, v_l refer to the easterly and northerly ADCP velocity components in the upper (subscript u) and lower (subscript l) layer and h_{diff} the vertical distance between layers. The direct effect of wind stress is usually confined to surface water, although indirect effects such as Ekman transport/overturning and the formation of eddies can facilitate currents and mixing at deeper depths (Cushman-Roisin and Beckers, 2011). The two-dimensional correlation coefficient R_{WC} between the
385 wind and ocean currents was calculated using Kundu, (1976) and the complex representations τ_c and u_c of the wind stress and de-tided current velocity vectors:

$$R_{WC} = \frac{\langle \tau_c^* u_c \rangle}{\langle \tau_c^* \tau_c \rangle^{\frac{1}{2}} \langle u_c^* u_c \rangle^{\frac{1}{2}}} \tag{E2}$$

where $\langle .. \rangle$ gives the normalized inner product of the vectors and * annotates the complex conjugate. We allow time-lags up to 15 hours to account for the gradual and indirect effects of wind stress on the ocean currents. Both properties were estimated
390 throughout the valid current velocity profile, but only down to 80 m depth due to the 8 m vertical distance between the defined layers used in the bulk velocity shear calculation.

Author contributions. Conceptualization: KOD,BF,AS,PL,PJ. Data curation: KOD,BF,MM. Formal Analysis: KOD,BF,MM. Funding acquisition: BF. Investigation: KOD, BF, AS. Methodology: KOD,BF. Project administration: BF, AS. Resources: BF. Software: KOD. Supervision: BF. Validation: n/a. Visualization: KOD,MM. Writing - original draft preparation: KOD. Writing - review & editing: KOD, BF, AS,
395   PL, PJ, MM.

Competing interests. The authors declare that they have no conflict of interest.

Acknowledgements. We thank the crew of R/V Helmer Hanssen during the deployment (CAGE 15-3) and recovery (CAGE 16-4) cruises. This study is a part of CAGE (Centre for Arctic Gas Hydrate, Environment and Climate), Norwegian Research Council grant no. 223259). We thank Nicholas Warner for proofreading the article.

400   **References**

Berchet, A., Bousquet, P., Pison, I., Locatelli, R., Chevallier, F., Paris, J.-D., Dlugokencky, E. J., Laurila, T., Hatakka, J., Viisanen, Y., Worthy,
       D. E. J., Nisbet, E., Fisher, R., France, J., Lowry, D., Ivakhov, V., and Hermansen, O.: Atmospheric constraints on the methane emissions
       from the East Siberian Shelf, Atmospheric Chemistry and Physics, 16, 4147–4157, https://doi.org/10.5194/acp-16-4147-2016, 2016.

Berndt, C., Feseker, T., Treude, T., Krastel, S., Liebetrau, V., Niemann, H., Bertics, V. J., Dumke, I., Dünnbier, K., Ferré, B., Graves, C.,
405   Gross, F., Hissmann, K., Hühnerbach, V., Krause, S., Lieser, K., Schauer, J., and Steinle, L.: Temporal Constraints on Hydrate-Controlled
       Methane Seepage off Svalbard, Science, 343, 284–287, https://doi.org/10.1126/science.1246298, 2014.

Beszczynska-Möller, A., Fahrbach, E., Schauer, U., and Hansen, E.: Variability in Atlantic water temperature and transport at the entrance to
       the Arctic Ocean, 1997–2010, ICES Journal of Marine Science, 69, 852–863, https://doi.org/10.1093/icesjms/fss056, 2012.

Braga, R., Iglesias, R., Romio, C., Praeg, D., Miller, D., Viana, A., and Ketzer, J.: Modelling methane hydrate stability changes and gas
410   release due to seasonal oscillations in bottom water temperatures on the Rio Grande cone, offshore southern Brazil, Marine and Petroleum
       Geology, 112, 104 071, https://doi.org/https://doi.org/10.1016/j.marpetgeo.2019.104071, 2020.

Canning, A., Fietzek, P., Rehder, G., and Körtzinger, A.: Technical note: Seamless gas measurements across the land–ocean aquatic con-
       tinuum – corrections and evaluation of sensor data for CO2, CH4 and O2 from field deployments in contrasting environments, Biogeo-
       sciences, 18, 1351–1373, https://doi.org/10.5194/bg-18-1351-2021, 2021.

415   Cottier, F., Nilsen, F., Inall, M. E., Gerland, S., Tverberg, V., and Svendsen, H.: Wintertime warming of an Arctic shelf in response to
       large-scale atmospheric circulation, Geophysical Research Letters, 34, https://doi.org/10.1029/2007GL029948, 2007.

Cushman-Roisin, B. and Beckers, J.-M.: Introduction to Geophysical Fluid Dynamics, vol. 101, Elsevier Academic Press, second edi edn.,
       2011.

Dee, D., Uppala, S., Simmons, A., Berrisford, P., Poli, P., Kobayashi, S., Andrae, U., Balmaseda, M., Balsamo, G., Bauer, P., Bechtold, P.,
420   Beljaars, A., van de Berg, L., Bidlot, J., Bormann, N., Delsol, C., Dragani, R., Fuentes, M., Geer, A., Haimberger, L., Healy, S., Hersbach,
       H., Hólm, E., Isaksen, L., Kållberg, P., Köhler, M., Matricardi, M., McNally, A., Monge-Sanz, B., Morcrette, J.-J., Park, B.-K., Peubey,
       C., de Rosnay, P., Tavolato, C., Thépaut, J.-N., and Vitart, F.: The ERA-Interim reanalysis: configuration and performance of the data
       assimilation system, Quarterly Journal of the Royal Meteorological Society, 137, 553–597, https://doi.org/10.1002/qj.828, 2011.

Dølven, K. O., Vierinen, J., Grilli, R., Trieste, J., and Férré, B.: Response time correction of slow response sensor data by deconvolution of
425   the growth-law equation, In prep.

Duan, Z. and Mao, S.: A thermodynamic model for calculating methane solubility, density and gas phase composition of methane-
       bearing aqueous fluids from 273 to 523 K and from 1 to 2000 bar, Geochimica et Cosmochimica Acta, 70, 3369–3386,
       https://doi.org/10.1016/j.gca.2006.03.018, 2006.

Etiope, G., Ciotoli, G., Schwietzke, S., and Schoell, M.: Gridded maps of geological methane emissions and their isotopic signature, Earth
430   System Science Data, 11, 1–22, https://doi.org/10.5194/essd-11-1-2019, 2019.

Ferré, B., Mienert, J., and Feseker, T.: Ocean temperature variability for the past 60 years on the Norwegian-Svalbard margin influences gas
       hydrate stability on human time scales, Journal of Geophysical Research: Oceans, 117, https://doi.org/10.1029/2012JC008300, 2012.

Ferré, B., Jansson, P., Moser, M., Portnov, A., Graves, C., Panieri, G., Gründger, F., Berndt, C., Lehmann, M., and Niemann,
       H.: Reduced methane seepage from Arctic sediments during cold bottom-water conditions, Nature Geoscience, 13, 144–148,
435   https://doi.org/10.1038/s41561-019-0515-3, 2020.

Franek, P., Plaza-Faverola, A., Mienert, J., Buenz, S., Ferré, B., and Hubbard, A.: Microseismicity Linked to Gas Migration and Leakage on the Western Svalbard Shelf, Geochemistry, Geophysics, Geosystems, 18, 4623–4645, https://doi.org/10.1002/2017GC007107, 2017.

Gentz, T., Damm, E., von Deimling, J. S., Mau, S., McGinnis, D. F., and Schlüter, M.: A water column study of methane around gas flares located at the West Spitsbergen continental margin, Continental Shelf Research, 72, 107–118, https://doi.org/10.1016/j.csr.2013.07.013, 2014.

Gerkema, T.: Tidal Constituents and the Harmonic Method, p. 60–86, Cambridge University Press, https://doi.org/10.1017/9781316998793.005, 2019.

Graves, C. A., Lea, S., Gregor, R., Niemann, H., Connely, D. P., Lowry, D., Fisher, R. E., Stott, A. W., Sahling, H., and James, R. H.: Fluxes and fate of dissolved methane released at the seafloor at the landward limit of the gas hydrate stability zone offshore western Svalbard, Journal of Geophysical Research: Oceans, 120, 6185–6201, https://doi.org/10.1002/2015JC011084, 2015.

Hanson, R. S. and Hanson, T. E.: Methanotrophic bacteria., Microbiological Reviews, I, 439–471, 1996.

Harvey, A. H.: Semiempirical correlation for Henry's constants over large temperature ranges, AIChE Journal, 42, 1491–1494, https://doi.org/10.1002/aic.690420531, 1996.

Hattermann, T., Erik, I. P., Wilken Jon, A., Jon, A., and Arild, S.: Eddy-driven recirculation of Atlantic Water in Fram Strait, Geophysical Research Letters, 43, 3406–3414, https://doi.org/10.1002/2016GL068323, 2016.

Hopkins, T. S.: The GIN Sea—A synthesis of its physical oceanography and literature review 1972–1985, Earth-Science Reviews, 30, 175–318, https://doi.org/https://doi.org/10.1016/0012-8252(91)90001-V, 1991.

Jansson, P., Ferré, B., Silyakova, A., Dølven, K. O., and Omstedt, A.: A new numerical model for understanding free and dissolved gas progression toward the atmosphere in aquatic methane seepage systems, Limnology and Oceanography: Methods, 17, 223–239, https://doi.org/10.1002/lom3.10307, 2019a.

Jansson, P., Triest, J., Grilli, R., Ferré, B., Silyakova, A., Mienert, J., and Chappellaz, J.: High-resolution underwater laser spectrometer sensing provides new insights into methane distribution at an Arctic seepage site, Ocean Science, 15, 1055–1069, https://doi.org/10.5194/os-15-1055-2019, 2019b.

Kossel, E., Bigalke, N., Piñero, E., and Haeckel, M.: The SUGAR Toolbox, https://doi.org/10.1594/PANGAEA.816333, 2013.

Kundu, P. K.: Ekman Veering Observed near the Ocean Bottom, Journal of Physical Oceanography, 6, 238–242, https://doi.org/10.1175/1520-0485(1976)006<0238:EVONTO>2.0.CO;2, 1976.

Large W. G. and Pond S.: Open Ocean Momentum Flux Measurements in Moderate to Strong Winds, Journal of Physical Oceanography, 11, 324–336, https://doi.org/10.1175/1520-0485(1981)011<0324:OOMFMI>2.0.CO;2, 1981.

Lincoln, B. J., Rippeth, T. P., and Simpson, J. H.: Surface mixed layer deepening through wind shear alignment in a seasonally stratified shallow sea, Journal of Geophysical Research: Oceans, 121, 6021–6034, https://doi.org/https://doi.org/10.1002/2015JC011382, 2016.

Linke, P., Sommer, S., Rovelli, L., and McGinnis, D. F.: Physical limitations of dissolved methane fluxes: The role of bottom-boundary layer processes, Marine Geology, 272, 209–222, https://doi.org/10.1016/j.margeo.2009.03.020, 2009.

Mau, S., Romer, M., Torres, M. E., Bussmann, I., Pape, T., Damm, E., Geprags, P., Wintersteller, P., Hsu, C.-W., Loher, M., and Bohrmann, G.: Widespread methane seepage along the continental margin off Svalbard - from Bjørnøya to Kongsfjorden, Scientific Reports, 7, 42 997, https://doi.org/10.1038/srep42997, 2017.

McDougall, T. J. and Barker, P. M.: Getting started with TEOS-10 and the Gibbs Seawater (GSW) Oceanographic Toolbox, SCOR/IAPSO WG127,, p. 22pp, 2011.

Saunois, M., Jackson, R. B., Bousquet, P., Poulter, B., and Canadell, J. G.: The growing role of methane in anthropogenic climate change, Environmental Research Letters, 11, 120 207, https://doi.org/10.1088/1748-9326/11/12/120207, 2016.

Saunois, M., R. Stavert, A., Poulter, B., Bousquet, P., G. Canadell, J., B. Jackson, R., A. Raymond, P., J. Dlugokencky, E., Houweling, S., K. Patra, P., Ciais, P., K. Arora, V., Bastviken, D., Bergamaschi, P., R. Blake, D., Brailsford, G., Bruhwiler, L., M. Carlson, K., Carrol, M., Castaldi, S., Chandra, N., Crevoisier, C., M. Crill, P., Covey, K., L. Curry, C., Etiope, G., Frankenberg, C., Gedney, N., I. Hegglin, M., Höglund-Isaksson, L., Hugelius, G., Ishizawa, M., Ito, A., Janssens-Maenhout, G., M. Jensen, K., Joos, F., Kleinen, T., B. Krummel, P., L. Langenfelds, R., G. Laruelle, G., Liu, L., MacHida, T., Maksyutov, S., C. McDonald, K., McNorton, J., A. Miller, P., R. Melton, J., Morino, I., Müller, J., Murguia-Flores, F., Naik, V., Niwa, Y., Noce, S., O'Doherty, S., J. Parker, R., Peng, C., Peng, S., P. Peters, G., Prigent, C., Prinn, R., Ramonet, M., Regnier, P., J. Riley, W., A. Rosentreter, J., Segers, A., J. Simpson, I., Shi, H., J. Smith, S., Paul Steele, L., F. Thornton, B., Tian, H., Tohjima, Y., N. Tubiello, F., Tsuruta, A., Viovy, N., Voulgarakis, A., S. Weber, T., Van Weele, M., R. Van Der Werf, G., F. Weiss, R., Worthy, D., Wunch, D., Yin, Y., Yoshida, Y., Zhang, W., Zhang, Z., Zhao, Y., Zheng, B., Zhu, Q., Zhu, Q., and Zhuang, Q.: The global methane budget 2000-2017, Earth System Science Data, 12, 1561–1623, https://doi.org/10.5194/essd-12-1561-2020, 2020.

Schlüter, M., Linke, P., and Suess, E.: Geochemistry of a sealed deep-sea borehole on the Cascadia Margin, Marine Geology, 148, 9–20, https://doi.org/https://doi.org/10.1016/S0025-3227(98)00016-4, 1998.

Shakhova, N., Semiletov, I., Leifer, I., Salyuk, A., Rekant, P., and Kosmach, D.: Geochemical and geophysical evidence of methane release over the East Siberian Arctic Shelf, Journal of Geophysical Research: Oceans, 115, https://doi.org/10.1029/2009JC005602, 2010.

Silyakova, A., Jansson, P., Serov, P., Ferré, B., Pavlov, A. K., Hattermann, T., Graves, C. A., Platt, S. M., Myhre, C. L., Gründger, F., and Niemann, H.: Physical controls of dynamics of methane venting from a shallow seep area west of Svalbard, Continental Shelf Research, 194, 104 030, https://doi.org/https://doi.org/10.1016/j.csr.2019.104030, 2020.

Sloan, E. D.: Physical/chemical properties of gas hydrates and application to world margin stability and climatic change, Geological Society, London, Special Publications,, 137, 31–50, 1998.

Sommer, S., Schmidt, M., and Linke, P.: Continuous inline mapping of a dissolved methane plume at a blowout site in the Central North Sea UK using a membrane inlet mass spectrometer – Water column stratification impedes immediate methane release into the atmosphere, Marine and Petroleum Geology, 68, 766–775, https://doi.org/10.1016/j.marpetgeo.2015.08.020, 2015.

Steinle, L., Graves, C., Treude, T., Ferre, B., Biastoch, A., Bussmann, I., Berndt, C., Krastel, S., James, R., Behrens, E., Böning, C., Greinert, J., Sapart, C., Scheinert, M., Sommer, S., Lehmann, M., and Niemann, H.: Water column methanotrophy controlled by a rapid oceanographic switch, Nature Geoscience, 8, 378–382, https://doi.org/10.1038/NGEO2420, 2015.

Tverberg, V., Nøst, O. A., Lydersen, C., and Kovacs, K. M.: Winter sea ice melting in the Atlantic Water subduction area, Svalbard Norway, Journal of Geophysical Research: Oceans, 119, 5945–5967, https://doi.org/10.1002/2014JC010013, 2014.

Veloso, M., Greinert, J., Mienert, J., and Batist, M.: A new methodology for quantifying bubble flow rates in deep water using splitbeam echosounders: Examples from the Arctic offshore NW-Svalbard, Limnology and Oceanography: Methods, 13, 267–287, 2015.

Veloso-Alarcón, M. E., Jansson, P., Batist, M. D., Minshull, T. A., Westbrook, G. K., Pälike, H., Bünz, S., Wright, I., and Greinert, J.: Variability of Acoustically Evidenced Methane Bubble Emissions Offshore Western Svalbard, Geophysical Research Letters, 46, 9072–9081, https://doi.org/10.1029/2019GL082750, 2019.

von Appen, W.-J., Schauer, U., Hattermann, T., and Beszczynska-Möller, A.: Seasonal Cycle of Mesoscale Instability of the West Spitsbergen Current, Journal of Physical Oceanography, 46, 1231–1254, https://doi.org/10.1175/JPO-D-15-0184.1, 2016.

Westbrook, G. K., Thatcher, K. E., Rohling, E. J., Piotrowski, A. M., Pälike, H., Osborne, A. H., Nisbet, E. G., Minshull, T. A., Lanoisellé, M., James, R. H., Hühnerbach, V., Green, D., Fisher, R. E., Crocker, A. J., Chabert, A., Bolton, C., Beszczynska-Möller, A., Berndt, C.,

and Aquilina, A.: Escape of methane gas from the seabed along the West Spitsbergen continental margin, Geophysical Research Letters,
550   36, https://doi.org/10.1029/2009GL039191, 2009.